Journal of Materials Chemistry A

Accepted Manuscript

Journal of
Materials Chemistry A

Materials for energy and sustainability

rsc.li/materials-a

Volume 6
Number 12
28 March 2018
Pages 4883-5230

ISSN 2050-7488

ROYAL SOCIETY OF CHEMISTRY

COMMUNICATION
Zhenhai Wen et al.
An electrochemically neutralized energy-assisted low-cost acid-alkaline electrolyzer for energy-saving electrolysis hydrogen generation

This is an Accepted Manuscript, which has been through the Royal Society of Chemistry peer review process and has been accepted for publication.

Accepted Manuscripts are published online shortly after acceptance, before technical editing, formatting and proof reading. Using this free service, authors can make their results available to the community, in citable form, before we publish the edited article. We will replace this Accepted Manuscript with the edited and formatted Advance Article as soon as it is available.

You can find more information about Accepted Manuscripts in the Information for Authors.

ROYAL SOCIETY OF CHEMISTRY

rsc.li/materials-a

Unraveling the Sodium Storage Mechanism in a Redox-Active Covalent Organic Framework Cathode for Na-Metal Batteries

Jonathan Caroni,[a,□] Asia Patriarchi,[b,□] Jon Otegi,[c] Leonardo Sbrascini,[d] Hegoi Manzano,[c] Javier Carrasco,[e,f] Manuel Souto,[a,g*] Miguel Ángel Muñoz-Márquez [b,d,h,*]

□ Authors contributed equally.

* Corresponding authors: miguel.munoz@inl.int, manuel.souto.salom@usc.es

[a] J. Caroni, Dr. M. Souto
     CiQUS, Centro Singular de Investigación en Química Bioloxica e Materiais Moleculares, Departamento de Química-Física,
     Universidade de Santiago de Compostela
     15782, Santiago de Compostela, Spain
     E-mail: manuel.souto.salom@usc.es

[b] A. Patriarchi, Dr. M. Á. Muñoz-Márquez
     School of Science and Technology; Chemistry division
     University of Camerino, via Madonna delle Carceri- ChIP
     62032 Camerino (MC), Italy

[c] J. Otegi, Dr. H. Manzano
     Department of Physics, University of the Basque Country (UPV/EHU)
     Sarriena auzoa, z.g., 48940 Leioa, Spain

[d] Dr. L. Sbrascini, Dr. M. Á. Muñoz-Márquez
     International Iberian Nanotechnology Laboratory
     Av. Mestre José Veiga, s/n
     4715-330 Braga, Portugal
     E-mail: miguel.munoz@inl.int

[e] Dr. J. Carrasco
     Centre for Cooperative Research on Alternative Energies (CIC Energigune), Basque Research and Technology Alliance (BRTA)
     Araba Technology Park, Albert Einstein 48, 01510 Vitoria-Gasteiz, Spain

[f] Dr. J. Carrasco
     IKERBASQUE, Basque Foundation for Science
     Plaza Euskadi 5, 48009 Bilbao, Spain

[g] Dr. M. Souto
     Oportunius, Galician Innovation Agency (GAIN),
     15702 Santiago de Compostela, Spain

[h] Dr. M. Á. Muñoz-Márquez
     National Reference Center for Electrochemical Energy Storage (GISEL)
     Via Giusti 9, 50121Firenze (FI), Italy.

Abstract: Sodium-based batteries are gaining increasing attention due to the abundant availability of sodium, among these, sodium-metal batteries (SMBs) are a promising solution. However, the development of suitable electrode materials for SMBs remains a significant challenge. Organic materials such as two-dimensional covalent organic frameworks (2D COFs) have emerged as promising electrodes due to their vast versatility, although their sodium storage mechanism remains poorly understood. In this work, the sodium storage mechanism of a β-ketoenamine anthraquinone-based COF (DAAQ-TFP), employed as a cathode for SMBs, is unveiled through a combination of electrochemical, physicochemical, and computational studies. In contrast with previous studies suggesting a capacitive storage mechanism, our results reveal a combination of pseudocapacitive and faradaic processes. Molecular dynamic simulations combined with *ex situ* X-ray diffraction studies confirmed that sodium storage occurs via interaction with carbonyl groups located within the COF channels rather than through intercalation between the COF layers. Moreover, electrode calendering experiments demonstrate that the faradaic contribution is governed by the porous COF structure. Finally, the redox inactivity of the carbonyl groups of the β-keto units is demonstrated through both computational and electrochemical measurements. These results further reinforce the role of anthraquinone units as the sole active sites responsible for sodium storage in this type of organic electrode materials.

Introduction

Lithium-ion batteries (LIBs) depend on critical raw materials, which are expensive and geographically concentrated in limited areas of the world, raising concerns over supply chain stability, cost evolution and mining environmental impact.[1,2] As the demand for sustainable energy storage grows, sodium-ion batteries, and particularly sodium-metal batteries (SMBs), are emerging as a promising alternative to LIBs, especially in the context of renewable energy sources integration.[3–5] Indeed, the interest in SMBs technology lies in the abundant, reduced environmental impact, enhanced energy density, and cost-effective nature of sodium.[6] Nonetheless, the larger atomic radius of sodium compared to lithium introduces significant challenges in the search for suitable electrode materials that can accommodate the structural deformations associated with sodium-ion insertion and extraction.[7] In this context, organic materials have emerged as promising candidates for the development of next-generation sodium-metal batteries due to their inherent structural tunability.[8–11] Among these, two-dimensional covalent organic frameworks (2D COFs) are porous organic polymers which are insoluble in battery electrolytes and can incorporate multiple electroactive moieties and conjugated linkers, enabling precise tuning of their electrochemical properties.[12–14] In particular, redox-active COFs have emerged as promising cathode materials for sodium ion storage.[12,15,16] Although some anthraquinone-based COFs have been previously studied as an anode in sodium-based batteries,[17] the detailed sodium storage mechanism in this type of COF-based electrode remains unclear.

In this work, the sodium-ion storage mechanism of a β-ketoenamine-linked anthraquinone-based COF (**DAAQ-TFP**) is unveiled, while its electrochemical performance as a positive electrode is evaluated. The performance of DAAQ-TFP has been benchmarked against other COF-based and anthraquinone-based organic cathodes reported for sodium-metal batteries (**Tables S1 and S2**), a wide range of specific capacity values is reported in the literature with the highest values corresponding to slow cycling rates. The DAAQ-TFP COF delivers very good values of capacity at the highest cycling rate reported along with retention values above 90% after almost 5000 cycles. However, the main aim of this work is to achieve a comprehensive understanding of the charge storage mechanism by evaluating the role of structure and morphology on the capacitive and faradaic processes occurring in **DAAQ-TFP**. Electrochemical impedance spectroscopy (EIS), cyclic voltammetry (CV), *ex-situ* X-ray diffraction (XRD) and molecular dynamics (MD) simulations are employed to determine the nature of ion interactions with the carbonyl groups located in the COF channels, while ruling out any intercalation process within the COF layers. The role of porosity in the faradaic component of ion storage is clarified by modulating the electrode porosity via calendering and experimentally characterizing it using small-angle X-ray scattering (SAXS). Finally, the electrochemical inactivity of the carbonyl groups of the β-keto units is demonstrated experimentally through electrochemical characterization and corroborated by density functional theory (DFT) calculations.

Results and Discussion

Synthesis and characterization of DAAQ-TFP

DAAQ-TFP COF was synthesized by adapting a reported solvothermal method, enabling the polymerization of 2,6-diaminoanthraquinone (DAAQ) and triformylphloroglucinol (TFP) in good yields (**Figure 1a**).[18,19] The simulated powder X-ray diffraction (PXRD) pattern from the model with AA stacking mode was found to be comparable to the experimental one, achieving a satisfactory Pawley refinement (**Figure 1b, Table S3**). To further validate the material's crystallinity and confirm the indexing of the reflection peaks, wide-angle X-ray scattering (WAXS) analysis was performed, revealing diffraction peaks at 3.5°, 5.9°, 7.0°, and 26.0°, which correspond to the (100), (110), (210), and (001) crystal planes, respectively (**Figure S1**). Fourier transform infrared spectroscopy (FTIR) was used to confirm the characteristic IR bands of **DAAQ-TFP** COF, showing intense bands at 1242 cm^{-1} and 1560 cm^{-1} related to C—N and C=C stretching vibrations, respectively. Additionally, the peak at 1618 cm^{-1} is attributed to the carbonyl stretching of the anthraquinone unit, in agreement with previous reports (**Figure S2**). [20]

The porous nature of **DAAQ-TFP** COF was investigated through N$_2$ adsorption and desorption isotherms at 77 K (**Figure S3**). The Brunauer-Emmett-Teller (BET) surface area was determined using the BETSI analysis, yielding a value of 984 m^2 g^{-1} with a pore size distribution in the range of 1.3-2.1 nm (**Figures S4-S5**).[21] To gain deeper insights into the porosity of the material, small-angle X-ray scattering (SAXS) analysis was conducted. The electron density contrast between the COF framework and its pores generates X-ray scattering, producing distinct peaks in the scattering vector (q) region. Low-q values correspond to larger pore sizes, while high-q values indicate smaller pores. The SAXS profile (**Figure 1c**) reveals microporosity and mesoporosity, as evidenced by the presence of peaks in the high-q region, with a primary peak at 2.5 nm^{-1}, alongside two additional peaks at 4.3 nm^{-1} and 5.2 nm^{-1}.[22] These values were used to determine the pore diameters of **DAAQ-TFP** (**Equation S1**), yielding values of 2.5, 1.5, and 1.2 nm, respectively. Notably, the pore sizes determined by SAXS and gas sorption measurements are in ful agreement.[23,24]

The thermal stability of **DAAQ-TFP** COF was confirmed by thermogravimetric analysis (TGA) performed under inert atmosphere (N$_2$) with significant mass loss only above 400°C (**Figure S6**).[25] Scanning electron microscopy (SEM) and Transmission Electron Microscopy (TEM) were performed to investigate the morphology and particle size of the material, revealing micrometre-sized particles (**Figures 1ed and S7a, S7b**). Energy-dispersive X-ray spectroscopy (EDX) further confirmed the homogeneous distribution of the expected elements present in the COF (**Table S4**).
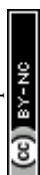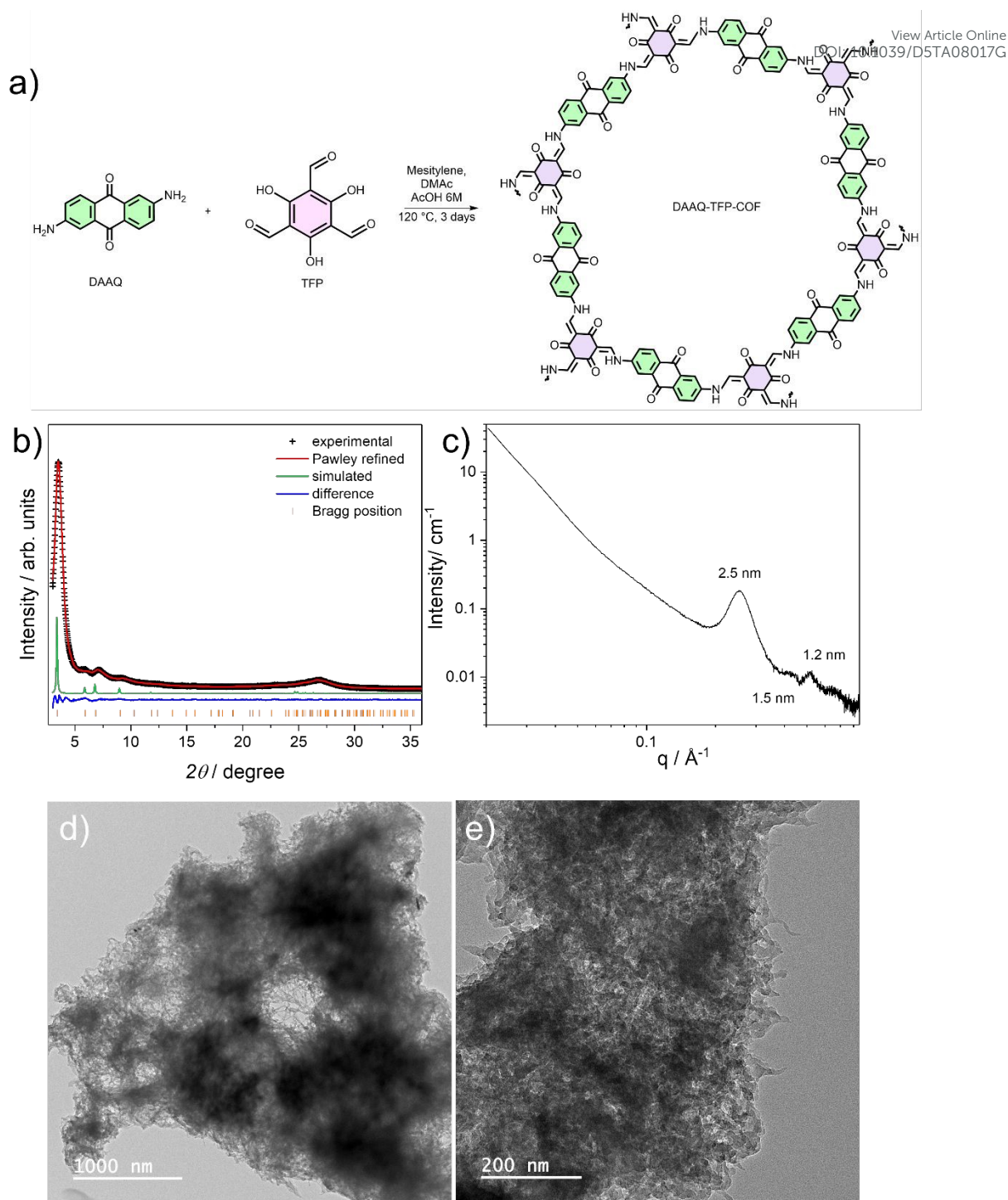
Figure 1. (a) Synthesis of DAAQ-TFP COF. (b) Experimental and simulated PXRD patterns of DAAQ-TFP-COF, and Pawley refinement. (c) SAXS analysis and pore size distribution of DAAQ-TFP-COF. (d, e) TEM images of DAAQ-TFP COF.

Charge storage mechanism

The sodium storage mechanism and diffusion kinetics were experimentally analysed through cyclic voltammetry (CV), as shown in **Figure S8**. The first three cycles are presented to provide insight into the evolution of the redox processes. During the anodic sweeps, only one peak should be expected, as observed in the storage process of lithium in the same molecule.[18] However, two well-defined oxidation peaks appear at approximately 1.50 V (labelled as A) and 1.95 V (labelled as B), which might be related to the redox activity of topologically different carbonyl groups in the DAAQ units.[18] The corresponding cathodic peaks (B' and A') during the reduction sweeps confirm the high reversibility of the redox reactions. Moreover, the consistent overlap of the CV curves upon cycling indicates a stable electrochemical behaviour, with no additional signals related to structural or compositional changes of the material.

To gain deeper insight into the sodium storage mechanism of **DAAQ-TFP**, CV measurements were performed at different scan rates, as shown in **Figure S9**. The curves maintain similar profiles across different rates, with only a slight increase in polarization observed at higher rates, indicating favourable reaction kinetics and stable electrochemical behaviour.[26] The contributions of both capacitive and faradaic (diffusion-controlled) processes were qualitatively evaluated using the power-law relationship ($I = av^b$) between the peak current (I) and the scan rate (v), by fitting the data to **Equation S2** and **Equation S3** [27,28], as shown in **Figure S10**. This approach is only valid if the peak current vs scan rate is linear, which is confirmed by the R^2 values obtained as shown in **Figure S11**. In general, a b value close to 0.5 suggests a diffusion-controlled process, characteristic of ion insertion/extraction between COF layers or channels, whereas a b value approaching 1 indicates a (pseudo)capacitive mechanism, mainly associated with surface reactions.[29] **Figure S10** illustrates the logarithmic relationship between the peak current and the scan rate, along with the corresponding linear fits. The calculated b values for peaks A and B in the anodic scans, as well as A' and B' in the cathodic scans, are in the range of 0.82 to 1.10, which supports a reaction mechanism mainly governed by surface-controlled reactions, likely due to sodium-ion adsorption at active sites.[30] It is worth noting that peaks A and A' exhibit a greater capacitive contribution compared to peaks B and B'. This difference will be discussed in more detail considering the EIS results. Meanwhile, the relationship between peak current and the square root of the scan rate (**Figure S12a**) displays a linear trend with $R^2 > 0.997$. This linearity likely arises from the presence of a faradaic contribution to sodium-ion storage, in addition to the capacitive mechanism described earlier, indicating a mixed pseudocapacitive behaviour. Accordingly, the Na^+ ion diffusion coefficients (D_{cv}) were determined by means of Randles–Sevčik method (**Equation S4**).[31] The obtained values of D_{CV} are reported in **Figure S12b**, showing sodium-ion diffusion coefficients in the order of 10^{-12} cm^2 s^{-1}, which are only slightly lower than those previously reported for the same **DAAQ-TFP** COF for lithium-ion battery (10^{-11} cm^2 s^{-1}).[18,32,33]

The capacitive contribution to the current response was quantified using the Dunn method, using **Equation S5**. [34,35] The current response $I(V)$ at a given potential can be deconvoluted into two distinct contributions: surface-controlled processes ($k_1 v$) and diffusion-dependent ($k_2 v^{1/2}$) contributions, where v represents the scan rate, and k_1 and k_2 are constants associated with each mechanism. By transforming **Equation S5** into its linear form (**Equation S6**), these parameters can be extracted, allowing for the quantification of their relative contributions to the storage mechanism. **Figure S13** illustrates the relative contributions of capacitive and faradaic processes at varying scan rates for peak A and B. As v increases, the capacitive contribution becomes more pronounced (due to reduced time for sodium-ion diffusion at high scan rates), confirming that the current response is largely governed by surface-induced processes.[36–38] Notably, peak A exhibits a consistently higher capacitive contribution across all scan rates, in agreement with the b values reported in **Figure S10**. By contrast, peak B demonstrates a stronger faradaic character, indicating some extent of Na^+ ion diffusion within the COF structure. These findings suggest that at ~1.50 V the dominant process is surface-controlled adsorption, whereas at ~1.95 V sodium storage also involves Na^+ insertion into the COF matrix. This is consistent with peak A being assigned to interaction of sodium ions with carbonyl groups located on the exterior of the COF, while peak B corresponds to the interaction of sodium ions with carbonyl groups within the COF pores.

To better define the charge storage mechanism of **DAAQ-TFP**, the interfacial behaviour of the material was further evaluated by impedance spectroscopy (see Supporting Information File and **Figure S14** for further details). The method used so far to identify the storage mechanisms is well established and widely used in the battery community. However, it is also known that the Dunn method may lack sufficient accuracy when dealing with ohmic drops, scan rate effects and complex systems that show capacitive and faradaic behaviour. This limitation can be overcome by performing advanced analysis of the EIS results to confirm the respective capacitive and faradaic contributions to the charge storage mechanism. To this end, multiple impedance measurements were acquired at selected SoCs during (de)sodiation, corresponding to the potential regions where electrochemical processes occur. Then, the complex impedance spectra (Z_{re} vs. $-Z_{im}$) were transformed into complex capacitance spectra (C_{re} vs. $-C_{im}$) by means of **Equation 1**, allowing simultaneous monitoring of both capacitance and impedance:[39,40]

$$C(\omega) = \frac{1}{j\omega Z(\omega)} \tag{1}$$

In line with the previous discussion, the $dQ\ dE^{-1}$ vs. E plot in **Figure 2a** highlights the two main processes occurring upon cycling: capacitive charge storage behaviour in the low-potential region (peaks A and A') and reversible faradaic diffusion-limited charge storage at high potentials (peaks B and B'). By comparing both complex capacitance and complex impedance dispersions (**Figure 2b-e**), a clear symmetry is discerned between the AC dispersions, according to the examined potential region. Measurements performed at peaks A and A' (**Figure 2b,d**) show a semicircle in the Cole-Cole capacitance plots and a blocking-like behaviour in the Nyquist impedance plots (insets). The blocking-like behaviour observed in the Nyquist diagram indicates minimal faradaic charge transfer, with the electrode behaving predominantly like a capacitor (charge accumulation without significant redox reactions). The presence of semicircles in the Cole-Cole diagrams, along with the blocking-like behaviour in the Nyquist, reflects relaxation processes associated with pseudocapacitive effects arising from double-layer formation. Deviations from ideal semicircles in the Cole-Cole diagram are ascribed to surface roughness or heterogeneities. Hence, the combination of limited faradaic contributions and capacitive relaxation processes strongly supports the assumption of a reversible capacitive-like behaviour at low potentials. Conversely, when observing peaks B and B' (**Figure 2c,e**), the Nyquist impedance data show a semicircular shape, indicating the presence of a finite charge-transfer resistance in parallel with capacitance, which is a hallmark of a faradaic electrochemical process. When converting the dispersions to the Cole-Cole capacitance diagrams (insets), a vertical "blocking-like" shape is displayed. This behaviour is not anomalous, as the extracted capacitance does not correspond to a true constant double-layer, but it rather reflects the interplay between the charge-transfer resistance and double-layer effects at the interfaces, the latter still being dominant. Under these assumptions, the system would indeed show a relatively vertical response in the capacitance domain even if the impedance data reveal the presence of a semicircular feature.[40–42] Hence, this supports the observation of a reversible faradaic contribution present at high potentials.

Finally, to evaluate the presence of multiple unconvoluted processes for all semi-circular features, the distribution of relaxation times (DRT) (**Figure 2g,i**), or distribution of differential capacitance (DDC) (**Figure 2f,h**), functions were calculated through Tikhonov regularization, as better illustrated in the Supporting Information section (**Figure S15**).[43] These findings, combined with the voltammetry measurements, unambiguously confirm the overall pseudocapacitive charge storage mechanism of **DAAQ-TFP** COF when used as a cathode material in SMBs: the current response in this system is the result of a charge storage mechanism similar to that of a conventional capacitor (apparent capacitance from a transient electrochemical double layer), but faradaic in nature (charge-transfer from an electrochemical redox reaction).[44]
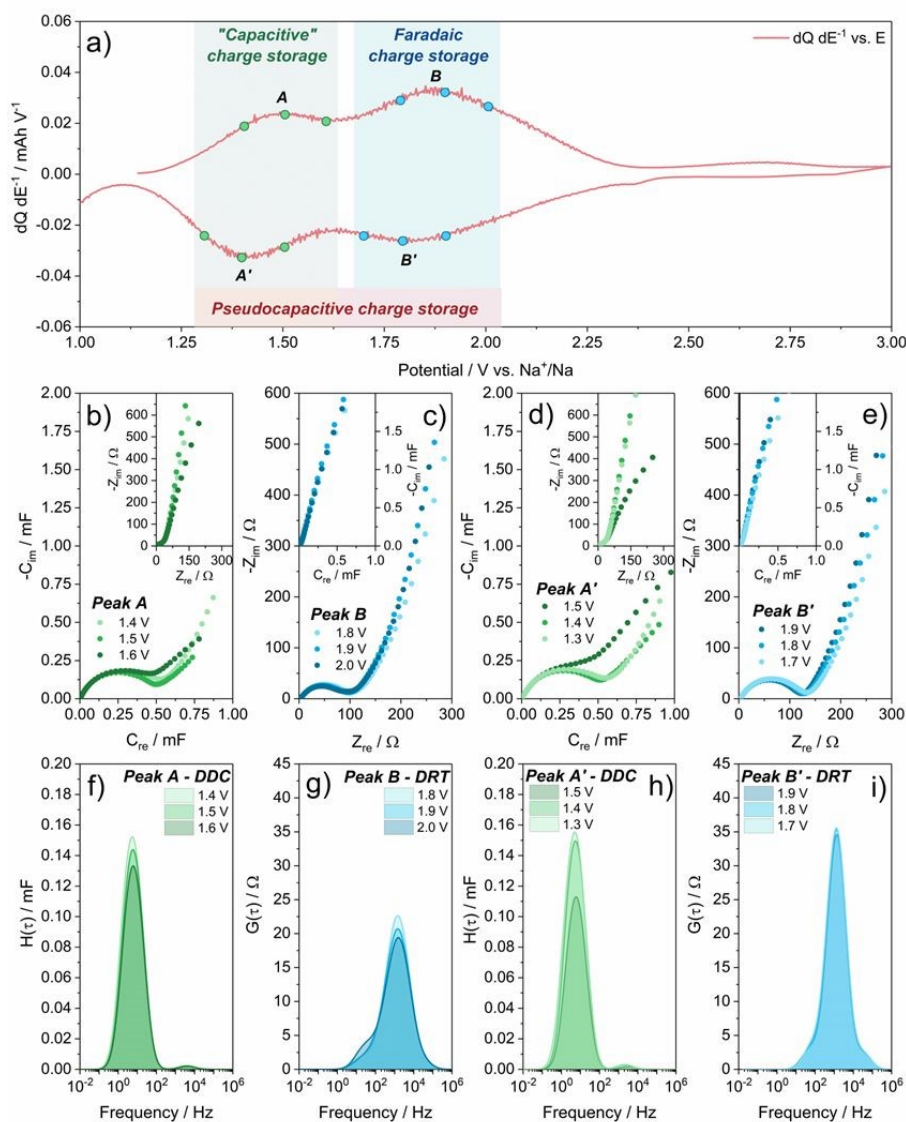
Figure 2. (a) dQ dE^{-1} vs E plot of the 10th galvanostatic cycle, highlighting the capacitive (green) and faradic (blue) regions, as well as the acquisition points for PEIS measurements. (b-e) Cole-Cole complex capacitance (green) and Nyquist complex impedance (blue) plots associated with the related potentials regions; (f-i) DDC (green) and DRT (blue) functions calculated from the semicircles in the Cole-Cole and Nyquist dispersions.

Hence, these features likely arise from the surface adsorption of Na$^+$ ions at the carbonyl groups in the organic framework, coupled to diffusion inside the open structure with faradaic reaction. To provide more insights on the sodium storage mechanisms, comparative ex-situ XRD analyses (**Figure 3a**) were conducted on pristine, sodiated, and desodiated electrodes, to determine whether sodium diffusion occurs through intercalation between layers or insertion through the stacked pores of the COF structure. The interlayer distance (*d*-spacing) was calculated using Bragg's Law (**Equation S7**) based on the peak corresponding to the (001) reflection, as summarized in **Table S5**. The obtained values, ranging from 3.4 to 3.5 Å, show no significant variation, suggesting that intercalation does not occur. This is further supported by prior studies on 2D materials, where ion intercalation is typically accompanied by a marked expansion of the interlayer spacing and, in some cases, structural exfoliation. For example, in graphite using sodium diglyme electrolytes, the pristine material displays a diffraction peak at 26.4°, corresponding to a *d*-spacing of 3.38 Å. Upon full sodiation, the most intense reflection shifts to 22.87°, indicating a periodic expansion to 11.65 Å— an effect that is clearly absent in our system, as better illustrated in the inset of **Figure 3a**.[45]

Furthermore, theoretical calculations support that Na$^+$ ions are preferentially confined within the pore channels of the COF structure, without intercalating between the stacked layers. DFT geometry optimizations yielded and interlayer distance of 3.3 Å, which increase up to 3.58±0.05 Å at room temperature MD simulations. On the other hand, **Figure 3b** depicts the distribution of sodium ions within the COF structure, showing distinct, non-overlapping spatial domains for each species: sodium is distributed along the COF channels, but the ions are never present in the interlayer space. Furthermore, **Figure S16** shows the distribution of the polar angle defined by the sodium ions and the different elements of the COF structure within the first sodium-coordination shell, as described in the SI. The distributions rapidly become negligible for polar angles lower than 45º and higher than 135º, indicating that sodium atoms are located parallel to the COF layers, rarely ever directly above or below them. We conclude from the MD trajectory analysis that the Na$^+$ is hosted within the COF structure but outside the interlayer region.
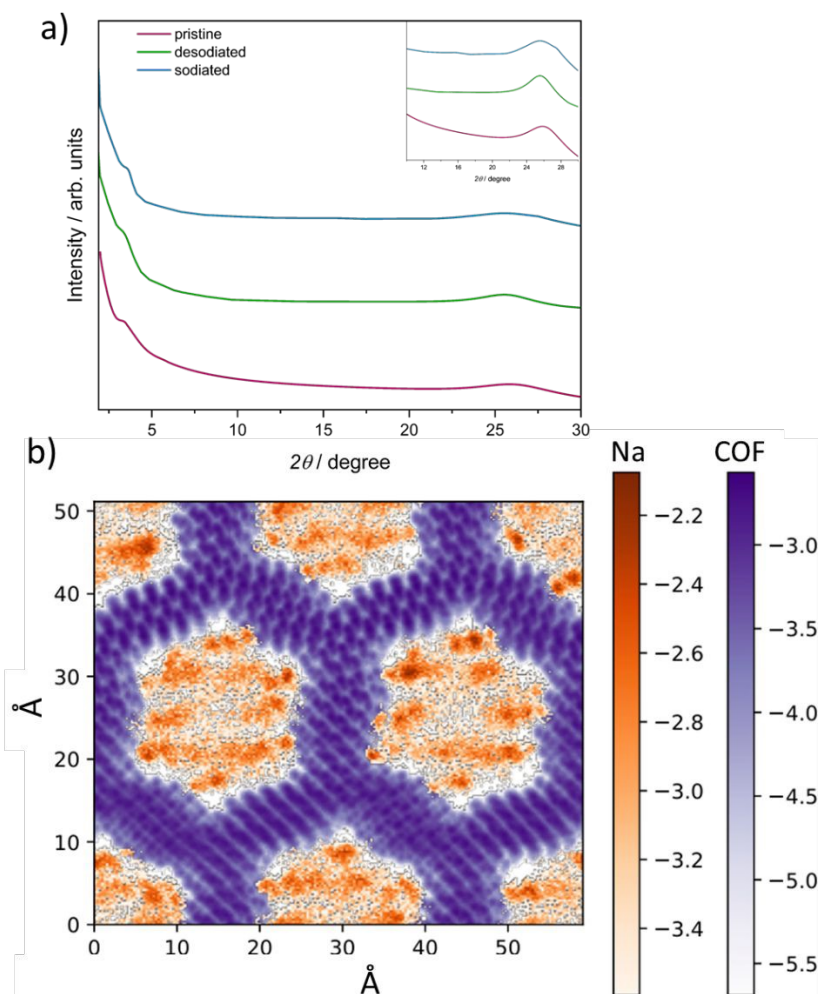
Figure 3. (a) PXRD patterns of the electrode at different states of charge: pristine (purple), sodiated (blue), and desodiated (green). Magnification of the 10-30º 2θ range in the inset. (b) Spatial distribution of sodium ions (orange) and COF atoms (purple) extracted from a 200 ns MD trajectory and projected onto the XY plane (parallel to the COF layers), represented as the logarithmic density distribution function.

Previous studies have reported a controversial role for the C=O groups of the β-keto units in the sodium storage mechanism.[17] To clarify this, we performed DFT calculations to investigate the storage mechanism at the atomic level. The model consisted of two layers of the **DAAQ-TFP** COF unit cell, comprising 6 DAAQ and 4 TFP units. **Figure S17** shows the electrostatic potential of the structure, defined as the sum of the Hartree potential and the local pseudopotential. Local minima are located near all oxygen atoms. Notably, deeper potential wells are observed near the anthraquinone oxygens compared to those near TFP units. **Figure S18** shows the electron density difference between the reduced and neutral COF structures, with the added charge clearly localized on the anthraquinone oxygen atoms. These results indicate the dominant role of DAAQ units in Na$^+$ storage.

To further explore Na$^+$ interaction with the COF, geometry optimizations across various sodiation stages was performed, following the workflow described next. **Figure 4a** illustrates the schematic reaction mechanism involved in the sodiation process of the **DAAQ-TFP** COF. For the first sodiation stage, the sodium atom was placed in two different sites. First, Na$^+$ was placed next to an oxygen atom of a DAAQ unit. After relaxation, it coordinates between the two COF layers, interacting with DAAQ oxygens in the adjacent plane (see **Figure 4b**). Second, the sodium atom was placed next to the TFP unit, and another geometry optimization was performed. Comparing the binding energy of both cases shows that the DAAQ-coordinated configuration is energetically more favourable. For the second sodiation stage, a second sodium atom was added near uncoordinated oxygen atoms, building various new configurations upon the most stable structure from the first stage. Following structural relaxations, the most energetically favourable configuration is revealed. Subsequent sodiation stages are constructed in a similar manner, positioning an additional Na atom to the previous stage configuration, next to uncoordinated oxygens. **Figure 4c** summarizes the calculated binding energies up to the seventh sodiation stage, consistently favouring DAAQ-coordinated configurations by at least 0.4 eV. The binding energy significantly increases at stage seven (over 30%), indicating a less favourable interaction, and corresponds to a TFP-coordinated configuration. However, upon extending our model to three COF layers, this trend is reversed, and DAAQ-coordination again becomes more stable, as depicted in **Figure S19**. At this stage, the DAAQ-coordinated configuration shows both binding energy and higher reduction potential, supporting a sequential Na$^+$ insertion with predicted 2:1 Na: DAAQ ratio for full sodiation. Furthermore, we can conclude that the Na$^+$ storage mechanism proceeds via stepwise coordination to DAAQ units, with negligible contribution from TFP units. This DAAQ preference in Na$^+$-COF interaction is further supported by MD simulations. The coordination number (CN) of Na$^+$ ions with DAAQ oxygen atoms is significantly higher

than TFP oxygens, 0.23 vs. 0.04, respectively (see **Figure S20**). **Figure S21** provides a clear, step-by-step visualization of the sodiation process in the DAAQ-TFP COF, offering improved clarity regarding the underlying electrochemical mechanism.

To further verify that carbonyl groups of the *b*-keto units do not influence the electrochemical performance of the **DAAQ-TFP** cathode, the TFP molecule was evaluated separately in a half-cell configuration. As shown in the cyclic voltammograms recorded at the 1st, 5th, 10th, and 20th cycles (**Figure S22a**), multiple redox peaks were detected. During the first cycle, a broad irreversible signal appears at approximately 0.75 V, which can be attributed to the formation of the solid electrolyte interphase. Two reversible peaks centered at 0.7 V and 0.01 V, corresponding to Na+ insertion and pore filling within the carbon matrix of C65 used as a conductive additive (30 wt%) in the electrode formulation, were observed (a CV measurement on just C65 and PVDF is reported in **Figure S23** for comparison). In contrast, the oxidation peak at 2.3 V, associated with the hydroxyl groups in TFP, lacks a corresponding reduction peak, indicating an electrochemically irreversible process. The progressive decline in its intensity over cycling further suggests a continuous loss of active functional groups. Charge/discharge tests (**Figure S22b**) reinforce the electrochemical inactivity of TFP, as evidenced by its low specific capacity and rapid capacity fading within just five cycles. Notably, although hydroxyl groups are present in the TFP molecule, they are eliminated during COF synthesis via condensation, meaning their electrochemical contribution is absent even in the initial cycles, confirming that TFP does not participate in the redox activity of the COF but only serves as structural binding bridges, enhancing the mechanical stability of the framework.

In addition, an analogous COF in which the anthraquinone moiety was replaced by an anthracene unit (denoted Da TFP-COF) was synthesized and fully characterized by PXRD, FTIR, and TGA (**Figures S24**, **S25** and **S26**). [46] The electrochemical performance of Da TFP-COF was evaluated under the same galvanostatic conditions used for **DAAQ-TFP** (0.3 A g^{-1}). As shown in **Figure S27a**, the cyclic voltammetry of Da TFP-COF, recorded at 0.2 mV s^{-1}, exhibits no significant redox features, in contrast to the pronounced redox peaks observed for **DAAQ-TFP**. This observation is consistent with the discharge profiles of Da TFP-COF in **Figure S27b**, obtained under the same conditions, which show a reversible capacity below 5 mAh g^{-1} over 1000 cycles, indicating negligible electrochemical activity. These results clearly confirm that the TFP moieties do not contribute to the charge-storage mechanism and that the electrochemical activity of **DAAQ-TFP** originates exclusively from the anthraquinone units.
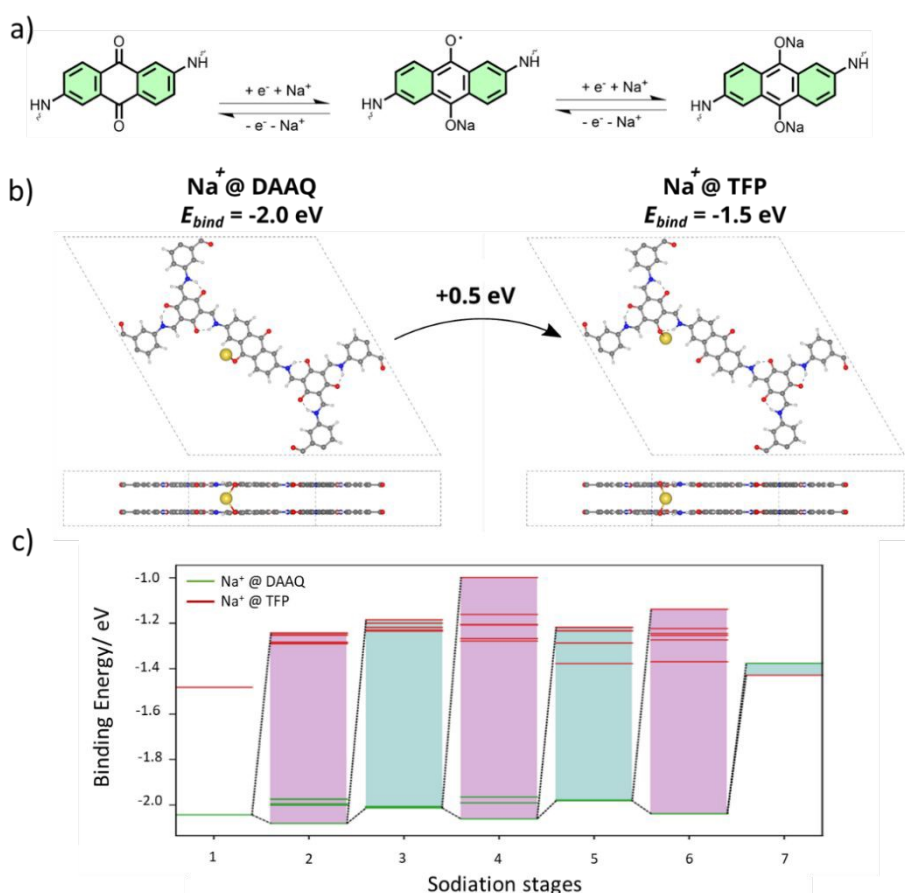

Figure 4. (a) Schematic representation of the sodiation mechanism of DAAQ-TFP COF. (b) Final binding energies and optimized configurations obtained from DFT-based geometry optimizations for two representative structures at the initial sodiation stage, side views in the insets. (c) Binding energies of sodium atoms at successive sodiation stages. Energy levels correspond to different structural configurations, with green and red markers indicating sodium coordination to oxygen atoms on DAAQ and TFP units, respectively.

Impact of porosity on the sodium storage mechanism

To further assess the influence of porosity on pseudocapacitive sodium-ion storage, the pristine electrode was calendered to reduce its thickness and increase its packing density, thereby limiting pore accessibility and modulating ion transport pathways. The morphological changes induced by a 50% reduction in the original electrode thickness were analysed via scanning electron microscopy, as shown in **Figure 5a,b**. The pristine electrode exhibits a highly porous texture with an interconnected network of voids, and loosely packed well-defined 3D structures. By contrast, after calendering, the electrode surface becomes significantly smoother and more compact, with a notable reduction in surface roughness. The compression-induced densification likely decreases ion-accessible active sites, possibly hindering sodium-ion diffusion towards COF channels. Indeed, following calendering, a loss of crystallinity in the COF structure was observed, as indicated by the PXRD patterns (**Figure 5c**). The characteristic low-angle diffraction peak, typically assigned to the (100) reflection, disappeared, while the peak at 26° remained visible but with significantly reduced intensity.

WAXS analysis confirmed the presence of the material's characteristic peaks (**Figure 5d**); however, they appeared broader and significantly less intense compared to the pristine electrode, indicating a reduction in crystallinity. The differences observed between the PXRD and WAXS patterns can be attributed to the distinct measurement geometries and sensitivities of the two techniques, since WAXS operates in transmission mode, whereas PXRD relies on Bragg-Brentano geometry. Despite these differences, both methods consistently indicate a loss of structural order, as reflected in the broadening and weakening of the characteristic COF diffraction peak.
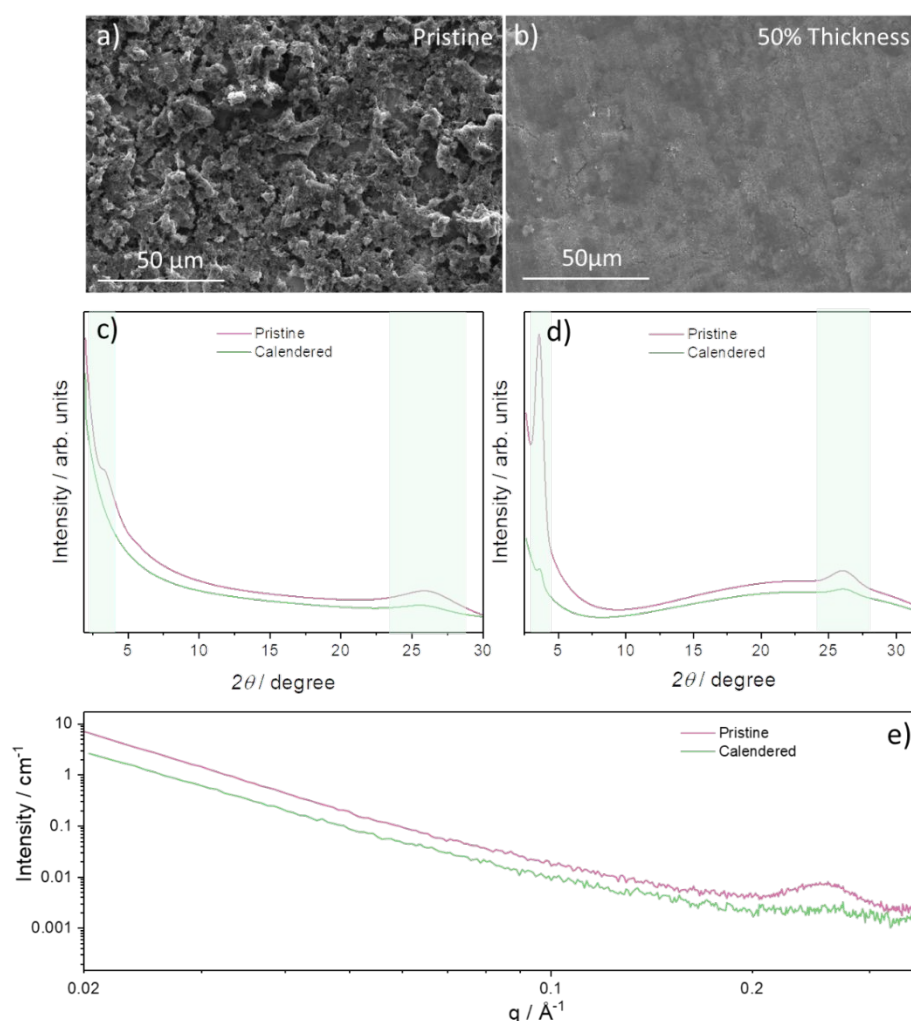

Figure 5. Structural characterization of the electrode before and after calendering. (a–b) SEM images of the pristine and calendered electrode, compressed to 50% of its original thickness. (c) PXRD patterns and (d) WAXS profiles comparing the structural features of the pristine and calendered electrodes. (e) Comparison of the pristine and calendered electrodes over an extended q range, encompassing the microporous region.

SAXS analysis, focused on the low-q region associated with grain-level structures, enabled the extraction of key structural parameters, including the radius of gyration (Rg), to elucidate differences between the two samples **(Figure S28 a,b)**. All fitting parameters are reported in **Table S4**, with the most relevant values discussed here.[47,48] The calendered electrode exhibited a higher cluster Rg compared to the pristine one (**Table S6**), indicating that the pristine sample is less compact and more loosely arranged at the aggregate level in the electrode. The increase in cluster size after calendering suggests the formation of larger, more interconnected aggregates. Conversely, the primary Rg value was lower in the pressed electrode implying that, after compression, the primary units, referring to the individual particles of the COF, have

become more compact or smaller. The mechanical force applied during pressing may have caused fragmentation or compaction of the COF particles. Furthermore, the mass fractal dimension significantly increased in the pressed electrode compared to the pristine one (**Table S6**), indicating a reduction in void spaces between particles, resulting in a more compacted material, with particles organized into a denser structure, increasing the mass distribution within the aggregate.

Analysis of the high-q region, which probes smaller structural features and porosity, further corroborates these findings. A pronounced decrease in the intensity of the first scattering peak was observed for the calendered electrode compared to the pristine sample (**Figure 5e**), reflecting a reduction in porosity as a result of the calendering process. Collectively, these findings point to a partial occlusion of the pores following calendering, potentially affecting the material's porosity and structural integrity, which would likely decrease ion-accessible active sites and hinder sodium-ion diffusion towards COF channels.[49] Therefore, the Na$^+$ storage mechanism of the calendered electrode was investigated through CV at different scan rates within the 1–3 V potential window (**Figure 6a**). Similar to the pristine sample, two distinct redox peaks are observed at approximately 1.5 and 1.9 V. However, the intensity ratio between these peaks is quite different when compared to the pristine electrode, suggesting a potential alteration in the sodium-ion storage mechanism induced by the densification process. [41]

Thus, the voltammograms were analysed using **Equations S2** and **S3**, following the power-law relationship between peak current and scan rate (**Figure S29a**). The logarithmic plot of peak current versus scan rate (**Figure S29b**) reveals *b* values close to 1, confirming the predominance of pseudocapacitive charge storage. Noteworthy, the *b* values for peaks A and A' are slightly lower than those observed for the pristine electrode. This decrease may be attributed to the reduction in surface-accessible pores following calendering, which limits the number of active sites available for Na$^+$ adsorption. As for the correlation between peak current and scan rate, a linear relationship (R² value of 0.99) is still observed for all redox peaks (**Figure S29a**). However, the analysis of peak current as a function of the square root of scan rate (**Figure S30**) exhibits a nonlinear dependence, indicating loss of significant faradaic contributions. These findings suggest that sodium-ion storage in the calendered electrode is primarily governed by a surface pseudocapacitive mechanism. When calendering, the pressure-induced structural modifications reduce the accessibility of the **DAAQ-TFP** COF's intrinsic channels to Na$^+$ ions, thereby disfavouring diffusion-driven insertion processes.

Electrochemical performance

To the best of our knowledge, this study presents the first evaluation of **DAAQ-TFP** COF for use as the cathode for sodium-metal batteries. The electrochemical performances of the material were assessed in coin cell configuration, employing sodium metal as the counter electrode and 1M NaPF$_6$ in DEGDME as electrolyte. Galvanostatic cycling was conducted at a current density of 2C (1C = 151 mAh g^{-1}) within the 1–3 V potential range, and the results are presented in **Figure 6b,c**. The pristine electrode demonstrated outstanding cycling stability, retaining a high specific capacity of approximately 120 mAh g^{-1} at 2C over 500 cycles with no significant capacity fade or failures, highlighting its potential application not only for lithium-ion batteries, as already reported in the literature, but also as a promising candidate for sodium-metal batteries in next-generation energy storage systems. [18,25,32,50]

To further investigate the influence of calendering on electrochemical performance, electrodes with varying thickness reduction (0–55%) were prepared, and their galvanostatic charge-discharge profiles at the 10th cycle are shown in **Figure 6b** for comparison. Long-term cycling over 500 charge/discharge cycles highlights the remarkable stability and high coulombic efficiency of all samples, reflecting the structural integrity of the COF framework (**Figure 6c**). However, increasing electrode compression led to a progressive decline in practical specific capacity, decreasing from 120 mAh g^{-1} for the pristine electrode to 45 mAh g^{-1} for the most compressed one. This reduction is likely attributed to hindered ion insertion, as pore collapse restricts access to the internal COF channels. Notably, at a 55% thickness reduction, the specific capacity dropped to nearly one-third of that of the uncompressed electrode, underscoring the crucial role of porosity in enabling effective sodium storage.

Rate capability tests were conducted to evaluate the influence of calendering-induced densification on the electrochemical performance of the material at different current densities. The electrodes were cycled at progressively increasing currents (C/10 to 2C) for 5 cycles each and eventually restoring the C/10 rate, to assess the material capacity recovery (**Figure S31**). The pristine electrode exhibited the highest performance, delivering an initial specific capacity of 140 mAh g^{-1} at C/10. A few activation cycles were required to stabilize the initial coulombic efficiency. Upon increasing the current density up to 2C, the capacity gradually declined and stabilized at 120 mAh g^{-1}, reflecting excellent rate capability and cycling stability. This behaviour is likely attributed to the combined contribution of pseudocapacitive and faradaic processes.[50] Notably, upon returning to C/10, the capacity was not only fully restored, but slightly enhanced (~150 mAh g^{-1}), highlighting the remarkable structural stability and reversibility of the COF. When the electrode underwent 25% and 35% thickness reduction, the electrochemical performance remained comparable, with specific capacities of ~125 mAh g^{-1} at C/10. The slight decrease compared to the pristine electrode suggests that moderate densification partially reduces Na$^+$ storage sites by compressing the COF's porous network. Nevertheless, good rate capability and capacity retention across different current densities are still exhibited. A more pronounced impact was observed at 50% volume reduction electrode, which suffered from lower CE at C/10 and a significant drop in performance, suggesting that excessive densification hinders Na$^+$ insertion by further restricting ion transport pathways within the **DAAQ-TFP** structure. At 55% thickness reduction, the electrochemical behaviour changed drastically. The specific capacity dropped substantially to ~45 mAh g^{-1} at C/10 and remained nearly constant across all current densities from C/5 to 2C. This plateau-like trend may suggest that Na$^+$ insertion into the COF framework was severely restricted, leading to a transition toward a surface-controlled capacitive process as the dominant charge storage mechanism. [51–53] Overall, an excessive compression of the pores (≥50%) seems to drastically limit Na$^+$ storage, leading to a severe loss of capacity compared to the pristine electrode.

Based on the reversible discharge at 0.3 A·g^{-1}, the **DAAQ-TFP** cathode delivers a gravimetric energy density of ≈195 Wh·kg^{-1}, consistent with values reported for organic redox polymers and COF-based electrodes (150–250 Wh·kg^{-1}), though lower than those of inorganic Na-metal cathodes. [1,32,54,55] Using the measured electrode area, loading, and thickness, the corresponding volumetric energy density is ≈32 Wh·L^{-1}, reflecting the intrinsically low density and high porosity of COF materials. Upon calendaring, the volumetric energy density more than doubled, demonstrating effective densification, albeit with a partial trade-off in electrochemical performance due to a reduced capacitive contribution.

Cathode utilization was further evaluated as a function of both C-rate and electrode densification, as shown in **Table S7** and **S8**. The results indicate that although calendering significantly enhances volumetric energy density, excessive densification increasingly limits ion transport and active-site accessibility, leading to reduced utilization. Galvanostatic charge–discharge profiles for the pristine electrode and electrodes with varying volume-reduction percentages resulting from calendaring are shown in **Figure S32**.
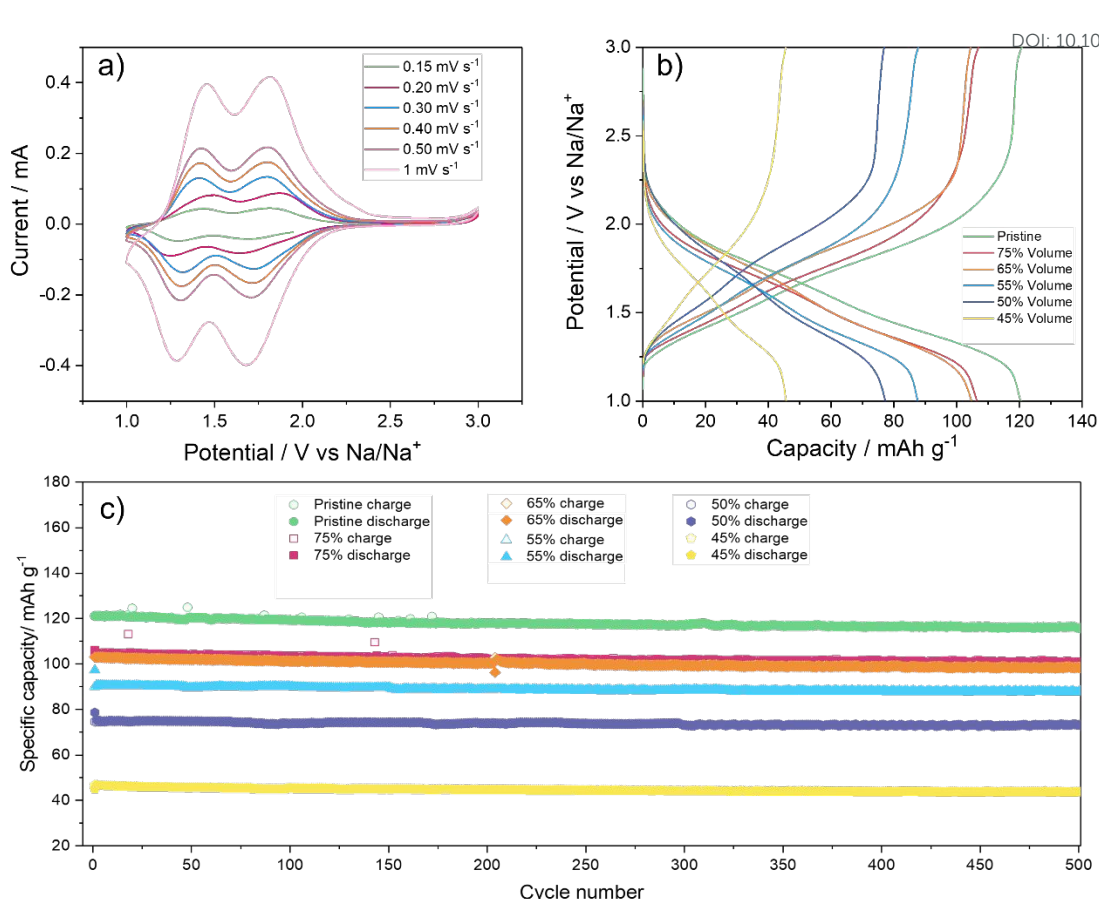
Figure 6. (a) Cyclic voltammetry of the DAAQ-TFP cathode recorded at different scan rates. (b) Galvanostatic charge–discharge profiles. (c) Long-term cycling performance over 500 cycles at a current rate of 2C, comparing the pristine electrode with calendered electrodes compressed to different volume percentages.

Ex-situ analysis

The exceptional electrochemical stability of the pristine electrode was further examined through *ex-situ* SEM analysis, as shown in **Figure S33**. Images acquired at different magnifications (**Figure S33a-f**) reveal that the electrode surface and morphology remain almost unchanged after 500 charge-discharge cycles. Notably, no signs of cracking, delamination, or structural degradation are observed, indicating a good mechanical integrity of the COF-based electrode as formulated. This morphological and textural preservation directly correlates with the outstanding electrochemical stability of the material, as the absence of deterioration may ultimately contribute to long-term cycling performance. Electrodes *ex-situ* XRD analysis reveals some extent of peak broadening, suggesting an increase in structural disorder relative to the pristine electrode, likely due to accumulated stress within the crystalline domains after prolonged electrochemical cycling. Nevertheless, the characteristic diffraction pattern of **DAAQ-TFP** is visible even after 500 cycles, highlighting its high structural stability during repeated cycling at high currents (**Figure S33g**).

Long-term cycling stability was further evaluated over an extensive 4775 charge/discharge cycles at a current density of 2C (**Figure 7a**), with performance compared against an electrode subjected to 50% volume reduction (**Figure S33**). After a brief activation phase, the pristine COF-based electrode demonstrated outstanding electrochemical stability, consistently delivering a specific capacity of approximately 120 mAh g^{-1} and maintaining a coulombic efficiency close to 100%. Notably, no signs of degradation, cell failure, or dendrite formation were observed throughout the test, underscoring the robustness of the material under prolonged cycling conditions. Remarkably, even after 4775 cycles, the electrode retained 91.2% of its initial capacity, with a coulombic efficiency reaching 99.99%, underscoring the remarkable structural robustness of the COF.

Ex-situ X-ray photoelectron spectroscopy (XPS) was performed on both pristine and cycled electrode to investigate the chemical composition of the cathode-electrolyte interphase (CEI). As shown in **Figure 7b-g**, both electrodes exhibit characteristic C 1s signals corresponding to the COF and the carbonaceous matrix of C65. Specifically, the spectra reveal the presence of C–C bonds at 284 eV, C=C and C–H bonds from graphitic-like structures at 285.5 eV, a C=O peak at 288.5 eV, and a C–F signal from the PVDF binder at 290.5 eV (**Figure 7b,c**).[56,57] The O 1s spectra (**Figure 7d,e**) further confirm these assignments, displaying complementary signals related to C–O bonds. However, after cycling, an additional peak emerges at approximately 537 eV, suggesting the formation of sodium fluorophosphate species, likely resulting from electrolyte decomposition.[58,59] This aligns well with the increased proportion of C–O bonds observed in the C 1s spectra after cycling. Notably, the F 1s spectra (**Figure 7f,g**) reveal significant changes upon cycling. Alongside the characteristic F–C bond at ~687 eV (corresponding to the C–F peak at 290.5 eV in the C 1s spectra), a new peak appears at around 685 eV, with an atomic percentage of 73%. This signal may be attributed to the formation of NaF, which is a key component in the CEI of Na-ion batteries.[60] The presence of a NaF-rich inorganic CEI is particularly beneficial, as NaF is known to enhance ionic conductivity, stabilizing the CEI, and mitigate side reactions between

Journal of Materials Chemistry A

the COF and the electrolyte.[7] Indeed, the formation of a stable CEI also helps suppress dendrite growth, thus contributing to the remarkable long-term stability observed upon cycling.[50]
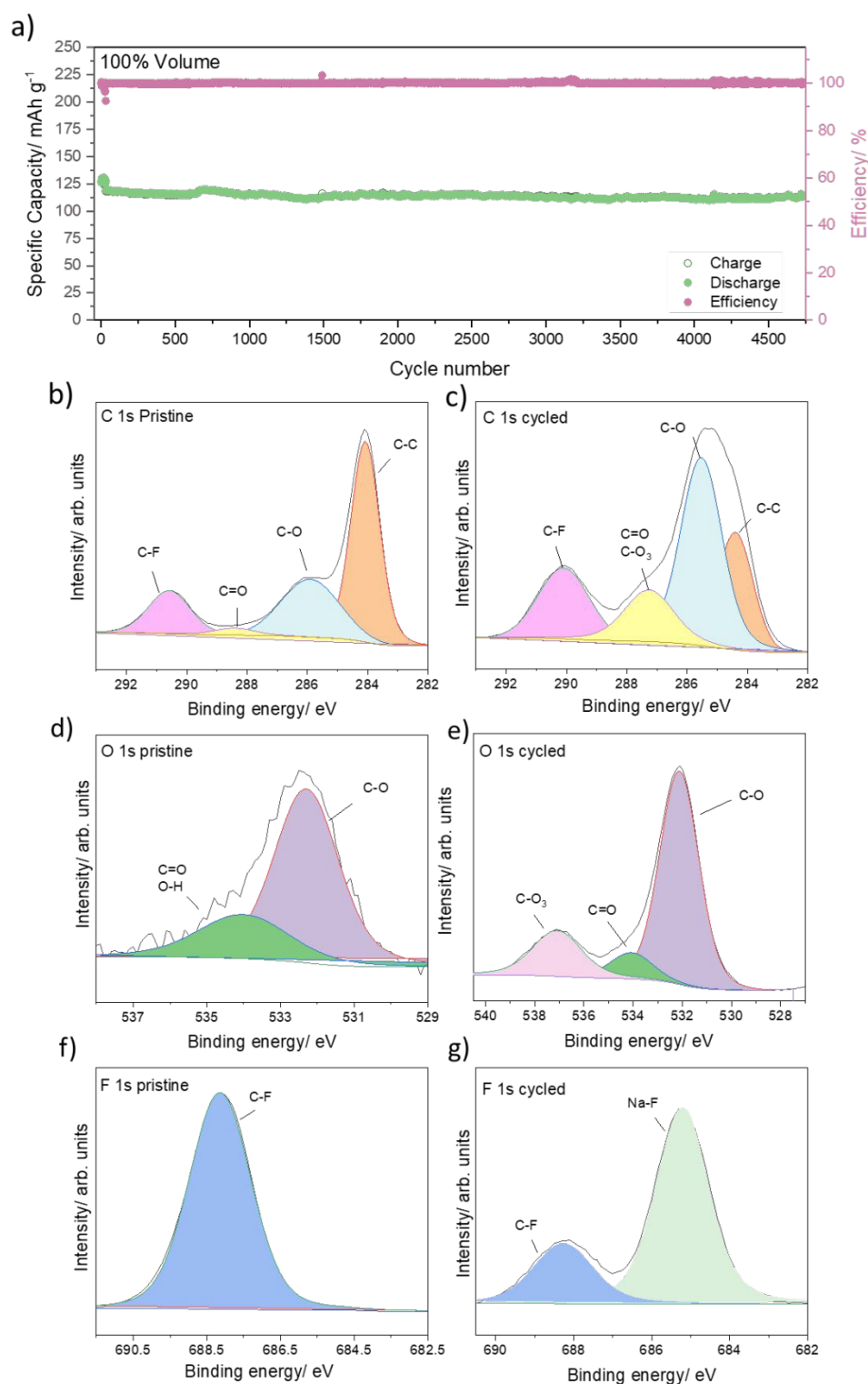
Figure 7. (a) Long-term cycling performance of the DAAQ-TFP cathode at a current density of 2C over 4900 cycles, illustrating both specific capacity and Coulombic efficiency. (b–g) XPS analysis comparing the surface chemical composition of the electrode before and after cycling: (b) C 1s spectrum of the pristine electrode; (c) C 1s spectrum after cycling; (d) O 1s spectrum of the pristine electrode; (e) O 1s spectrum after cycling; (f) F 1s spectrum of the pristine electrode; (g) F 1s spectrum after cycling.

Ex-situ Raman spectroscopy was performed on the **DAAQ-TFP** COF at selected potentials (3.0, 2.0, and 1.0 V vs. Na/Na+) to monitor structural changes associated with sodiation (**Figure 8a**). Particular attention was given to the C=O stretching region (**Figure 8b**). When the electrode is sodiated and then fully de-sodiated (3.0 V), the C=O vibration appears at 1660 cm−1; upon discharge to 2.0 V, this band shifts to 1658 cm−1, and further sodiation to 1.0 V results in a final shift to 1657 cm−1. This progressive red-shift of the carbonyl stretching mode is

consistent with the coordination of Na⁺ to the carbonyl oxygen atoms, which weakens the C=O double bond and lowers its vibrational energy. In parallel, peak broadening is observed: the full width at half maximum increases from 12.48 cm⁻¹ (3.0 V) to 14.40 cm⁻¹ (2.0 V) and 14.65 cm⁻¹ (1.0 V). Such broadening is typically attributed to increasing structural disorder and a distribution of Na⁺-O coordination environments during ion uptake, therefore indicating that carbonyl groups act as the redox-active coordination sites for reversible Na⁺ storage in the **DAAQ-TFP** framework. [61–63]
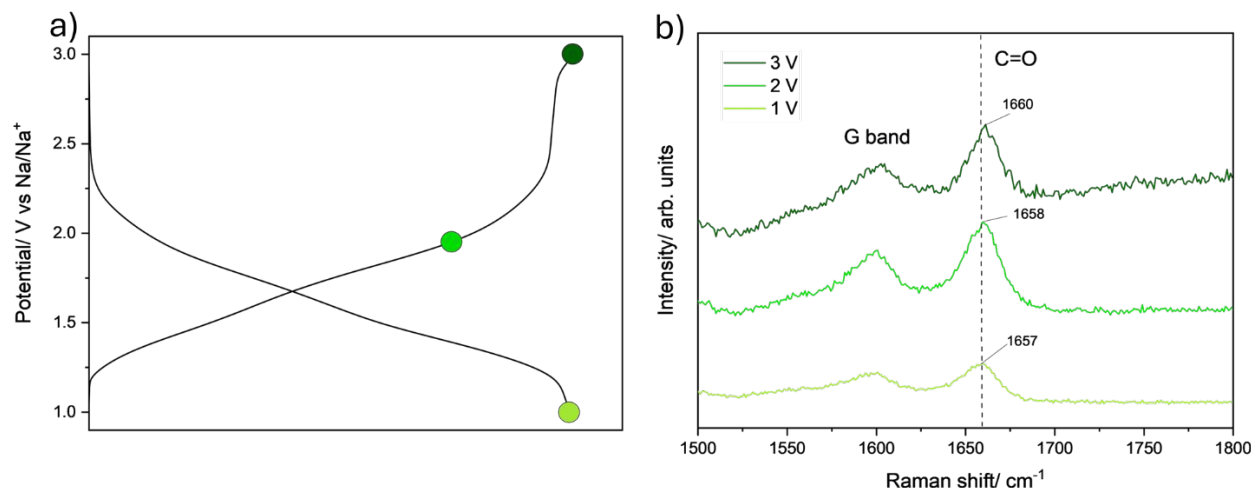
Figure 8. Ex-situ Raman measurements performed on DAAQ-TFP at (a) 3 V and after discharging to 2 V and 1 V, with focus (b) on the C=O region.

Conclusion

In this study, the electrochemical behaviour of **DAAQ-TFP** COF as an organic cathode material for sodium-metal batteries was systematically investigated for the first time. A comprehensive characterization, including X-ray diffraction, small-angle X-ray scattering, cyclic voltammetry, and electrochemical impedance spectroscopy, as well as DFT-based electronic structure calculations and classical MD simulations, was employed to elucidate the sodium storage mechanism in this material, which, up to date, had remained controversial. The results confirmed that the redox process involves two distinct contributions: one associated with a surface-controlled capacitive mechanism and the other governed by a pseudocapacitive insertion process with a faradaic contribution. Furthermore, the effect of electrode densification through calendering was evaluated, revealing that compression hindered sodium-ion diffusion by reducing pore accessibility. The pristine electrode exhibited outstanding cycling performance, maintaining 91.2% of its initial capacity after almost 4800 charge/discharge cycles at 2C, with nearly 100% coulombic efficiency. Although **DAAQ-TFP** COF exhibits a moderate theoretical capacity (151 mAh·g⁻¹) and operating voltage, it achieves exceptionally high utilization (≈145 mAh·g⁻¹ at C/10) and retains outstanding rate capability (≈120 mAh·g⁻¹ at 2C), along with excellent cycling stability and robust structural integrity. Importantly, the goal of this work is not merely to maximize electrochemical performance, but to elucidating the sodiation mechanism within the COF, thereby providing fundamental insights that support the advancement of COF-based materials for realistic sodium–organic battery applications. These findings highlight the great potential of **DAAQ-TFP** COF as a promising cathode material for next-generation sodium-organic batteries.

Conflicts of interest

There are no conflicts to declare

Data availability

The data supporting this article have been included as part of the Supplementary Information.

Acknowledgements

Keywords: covalent organic framework • sodium-metal battery • sodium storage mechanism • organic batteries

References

[1] R. Usiskin, Y. Lu, J. Popovic, M. Law, P. Balaya, Y. S. Hu, J. Maier, *Nat Rev Mater* 2021, *6*, DOI 10.1038/s41578-021-00324-w.

[2] B. Dunn, H. Kamath, J. M. Tarascon, *Science (1979)* 2011, *334*, DOI 10.1126/science.1212741.

[3] X. Dou, I. Hasa, D. Saurel, C. Vaalma, L. Wu, D. Buchholz, D. Bresser, S. Komaba, S. Passerini, *Materials Today* 2019, *23*, DOI 10.1016/j.mattod.2018.12.040.

[4] H. Moon, A. Innocenti, H. Liu, H. Zhang, M. Weil, M. Zarrabeitia, S. Passerini, *ChemSusChem* 2023, *16*, DOI 10.1002/cssc.202201713.

[5] D. Larcher, J. M. Tarascon, *Nat Chem* 2015, *7*, DOI 10.1038/nchem.2085.

[6] H. Gao, W. Zhou, K. Park, J. B. Goodenough, *Adv Energy Mater* 2016, *6*, DOI 10.1002/aenm.201600467.

[7] A. Patriarchi, J. Caroni, L. Minnetti, L. Sbrascini, H. Darjazi, F. Nobili, M. Á. Muñoz-Márquez, *ChemElectroChem* 2025, DOI 10.1002/celc.202400350.

[8] Q. Zhao, Y. Lu, J. Chen, *Adv Energy Mater* 2017, *7*, DOI 10.1002/aenm.201601792.

[9] H. Zhang, Y. Gao, X. H. Liu, Z. Yang, X. X. He, L. Li, Y. Qiao, W. H. Chen, R. H. Zeng, Y. Wang, S. L. Chou, *Adv Funct Mater* 2022, *32*, DOI 10.1002/adfm.202107718.

[10] H. Lyu, X. G. Sun, S. Dai, *Advanced Energy and Sustainability Research* 2021, *2*, DOI 10.1002/aesr.202000044.

[11] R. Dantas, C. Ribeiro, M. Souto, *Chem. Commun.* 2023, *60*, DOI 10.1039/d3cc04322c.

[12] L. Kong, M. Liu, H. Huang, Y. Xu, X. H. Bu, *Adv Energy Mater* 2022, *12*, DOI 10.1002/aenm.202100172.

[13] C. Ribeiro, R. Markowski, R. F. Mendes, A. Fernández-Alarcón, J. Calbo, J. Rocha, A. Vlad, M. Souto, *Batter Supercaps* 2025, DOI 10.1002/batt.202500360.

[14] N.d.

[15] C. Zhang, C. Lu, F. Zhang, F. Qiu, X. Zhuang, X. Feng, *Journal of Energy Chemistry* 2018, *27*, DOI 10.1016/j.jechem.2017.11.008.

[16] W. Yuan, J. Weng, M. Ding, H. M. Jiang, Z. Fan, Z. Zhao, P. Zhang, L. P. Xu, P. Zhou, *Energy Storage Mater* 2024, *65*, DOI 10.1016/j.ensm.2023.103142.

[17] S. Gu, S. Wu, L. Cao, M. Li, N. Qin, J. Zhu, Z. Wang, Y. Li, Z. Li, J. Chen, Z. Lu, *J Am Chem Soc* 2019, *141*, DOI 10.1021/jacs.9b03467.

[18] S. Wang, Q. Wang, P. Shao, Y. Han, X. Gao, L. Ma, S. Yuan, X. Ma, J. Zhou, X. Feng, B. Wang, *J Am Chem Soc* 2017, *139*, DOI 10.1021/jacs.7b02648.

[19] C. R. Deblase, K. E. Silberstein, T. T. Truong, H. D. Abruña, W. R. Dichtel, *J Am Chem Soc* 2013, *135*, DOI 10.1021/ja409421d.

[20] O. Lužanin, R. Dantas, R. Dominko, J. Bitenc, M. Souto, *J Mater Chem A Mater* 2023, *11*, DOI 10.1039/d3ta05190k.

[21] J. W. M. Osterrieth, J. Rampersad, D. Madden, N. Rampal, L. Skoric, B. Connolly, M. D. Allendorf, V. Stavila, J. L. Snider, R. Ameloot, J. Marreiros, C. Ania, D. Azevedo, E. Vilarrasa-Garcia, B. F. Santos, X. H. Bu, Z. Chang, H. Bunzen, N. R. Champness, S. L. Griffin, B. Chen, R. B. Lin, B. Coasne, S. Cohen, J. C. Moreton, Y. J. Colón, L. Chen, R. Clowes, F. X. Coudert, Y. Cui, B. Hou, D. M. D'Alessandro, P. W. Doheny, M. Dincă, C. Sun, C. Doonan, M. T. Huxley, J. D. Evans, P. Falcaro, R. Ricco, O. Farha, K. B. Idrees, T. Islamoglu, P. Feng, H. Yang, R. S. Forgan, D. Bara, S. Furukawa, E. Sanchez, J. Gascon, S. Telalović, S. K. Ghosh, S. Mukherjee, M. R. Hill, M. M. Sadiq, P. Horcajada, P. Salcedo-Abraira, K. Kaneko, R. Kukobat, J. Kenvin, S. Keskin, S. Kitagawa, K. ichi Otake, R. P. Lively, S. J. A. DeWitt, P. Llewellyn, B. V. Lotsch, S. T. Emmerling, A. M. Pütz, C. Martí-Gastaldo, N. M. Padial, J. García-Martínez, N. Linares, D. Maspoch, J. A. Suárez del Pino, P. Moghadam, R. Oktavian, R. E. Morris, P. S. Wheatley, J. Navarro, C. Petit, D. Danaci, M. J. Rosseinsky, A. P. Katsoulidis, M. Schröder, X. Han, S. Yang, C. Serre, G. Mouchaham, D. S. Sholl, R. Thyagarajan, D. Siderius, R. Q. Snurr, R. B. Goncalves, S. Telfer, S. J. Lee, V. P. Ting, J. L. Rowlandson, T. Uemura, T. Iiyuka, M. A. van der Veen, D. Rega, V. Van Speybroeck, S. M. J. Rogge, A. Lamaire, K. S. Walton, L. W. Bingel, S. Wuttke, J. Andreo, O. Yaghi, B. Zhang, C. T. Yavuz, T. S. Nguyen, F. Zamora, C. Montoro, H. Zhou, A. Kirchon, D. Fairen-Jimenez, *Advanced Materials* 2022, *34*, DOI 10.1002/adma.202201502.

[22] R. A. Maia, L. S. D. A. Carneiro, J. M. C. Cifuentes, C. D. Buarque, P. M. Esteves, A. M. Percebom, *J Appl Crystallogr* 2020, *53*, DOI 10.1107/S1600576720011553.

[23] A. P. Radlinski, M. Mastalerz, A. L. Hinde, M. Hainbuchner, H. Rauch, M. Baron, J. S. Lin, L. Fan, P. Thiyagarajan, *Int J Coal Geol* 2004, *59*, DOI 10.1016/j.coal.2004.03.002.

[24] Y. Zhao, L. Peng, S. Liu, B. Cao, Y. Sun, B. Hou, *Mar Pet Geol* 2019, *102*, DOI 10.1016/j.marpetgeo.2018.12.041.

[25] F. Lv, S. Xiong, J. Zhang, X. Wang, J. Chu, R. Zhang, M. Gong, B. Wu, G. Liu, W. Luo, *Electrochim Acta* 2021, *398*, DOI 10.1016/j.electacta.2021.139301.

[26] H. Zhang, I. Hasa, S. Passerini, *Adv Energy Mater* 2018, *8*, DOI 10.1002/aenm.201702582.

[27] V. Augustyn, J. Come, M. A. Lowe, J. W. Kim, P. L. Taberna, S. H. Tolbert, H. D. Abruña, P. Simon, B. Dunn, *Nat Mater* 2013, *12*, DOI 10.1038/nmat3601.

[28] E. Wierzbinski, R. Venkatramani, K. L. Davis, S. Bezer, J. Kong, Y. Xing, E. Borguet, C. Achim, D. N. Beratan, D. H. Waldeck, *ACS Nano* 2013, *7*, DOI 10.1021/nn401321k.

[29] J. Wang, J. Polleux, J. Lim, B. Dunn, *Journal of Physical Chemistry C* 2007, *111*, DOI 10.1021/jp074464w.

[30] Y. Du, Y. Qiu, R. Zhuang, X. Jing, D. Liu, X. Peng, L. Yan, F. Xu, *Carbon N Y* 2024, *221*, DOI 10.1016/j.carbon.2024.118929.

[31] J. E. B. Randles, *Faraday Discuss* 1947, *1*, DOI 10.1039/DF9470100011.

[32] L. Zhang, X. Zhang, D. Han, L. Zhai, L. Mi, *Small Methods* 2023, *7*, DOI 10.1002/smtd.202300687.

[33] H. Wang, W. Zou, C. Liu, Y. Sun, Y. Xu, W. Sun, Y. Wang, *Batter Supercaps* 2023, *6*, DOI 10.1002/batt.202200434.

[34] M. Forghani, S. W. Donne, *J Electrochem Soc* 2018, *165*, DOI 10.1149/2.0931803jes.

[35] A. F. Dunn, *Can J Phys* 1964, *42*, DOI 10.1139/p64-005.

[36] Y. Lan, H. Zhao, Y. Zong, X. Li, Y. Sun, J. Feng, Y. Wang, X. Zheng, Y. Du, *Nanoscale* 2018, *10*, DOI 10.1039/c8nr01229f.

[37] Y. Li, Y. Meng, M. Xiao, X. Liu, F. Zhu, Y. Zhang, *Journal of Materials Science: Materials in Electronics* 2019, *30*, DOI 10.1007/s10854-019-01629-x.

[38] L. Zhang, T. Wei, Z. Jiang, C. Liu, H. Jiang, J. Chang, L. Sheng, Q. Zhou, L. Yuan, Z. Fan, *Nano Energy* 2018, *48*, DOI 10.1016/j.nanoen.2018.03.053.

[39] C. Gu, L. Yin, S. Li, B. Zhang, X. Liu, T. Yan, *Electrochim Acta* 2021, *367*, DOI 10.1016/j.electacta.2020.137517.

[40]   M. Itagaki, S. Suzuki, I. Shitanda, K. Watanabe, *Electrochemistry* 2007, *75*, DOI 10.5796/electrochemistry.75.649.
[41]   T. Schoetz, L. W. Gordon, S. Ivanov, A. Bund, D. Mandler, R. J. Messinger, *Electrochim Acta* 2022, *412*, DOI 10.1016/j.electacta.2022.140072.
[42]   J. Wang, Q. A. Huang, W. Li, J. Wang, Y. Bai, Y. Zhao, X. Li, J. Zhang, *Journal of Electroanalytical Chemistry* 2022, *910*, DOI 10.1016/j.jelechem.2022.116176.
[43]   A. L. Gavrilyuk, D. A. Osinkin, D. I. Bronin, *Russian Journal of Electrochemistry* 2017, *53*, DOI 10.1134/S1023193517060040.
[44]   K. Amin, J. Zhang, H. Y. Zhou, R. Lu, M. Zhang, N. Ashraf, C. Yueli, L. Mao, C. F. J. Faul, Z. Wei, *Sustain Energy Fuels* 2020, *4*, DOI 10.1039/d0se00610f.
[45]   N. Karimi, A. Varzi, S. Passerini, *Electrochim Acta* 2019, *304*, DOI 10.1016/j.electacta.2019.03.036.
[46]   M. A. Khayum, S. Kandambeth, S. Mitra, S. B. Nair, A. Das, S. S. Nagane, R. Mukherjee, R. Banerjee, *Angewandte Chemie - International Edition* 2016, *55*, DOI 10.1002/anie.201607812.
[47]   P. W. Schmidt, *J Appl Crystallogr* 1991, *24*, DOI 10.1107/S0021889891003400.
[48]   A. J. Hurd, D. W. Schaefer, J. E. Martin, *Phys Rev A (Coll Park)* 1987, *35*, DOI 10.1103/PhysRevA.35.2361.
[49]   C. Matei Ghimbeu, J. Górka, V. Simone, L. Simonin, S. Martinet, C. Vix-Guterl, *Nano Energy* 2018, *44*, DOI 10.1016/j.nanoen.2017.12.013.
[50]   G. Ren, F. Cai, S. Wang, Z. Luo, Z. Yuan, *RSC Adv* 2023, *13*, DOI 10.1039/d3ra01414b.
[51]   Y. Wu, H. Chen, H. Wang, J. Liu, Q. He, L. Que, X. Wang, F. Yu, J. Meng, C. Lu, Y. Xie, *J Energy Storage* 2024, *98*, DOI 10.1016/j.est.2024.113162.
[52]   Z. Li, Y. Xiang, S. Lu, B. Dong, S. Ding, G. Gao, *J Alloys Compd* 2018, *737*, DOI 10.1016/j.jallcom.2017.11.336.
[53]   Y. Xiang, H. Wu, K. H. L. Zhang, M. Coto, T. Zhao, S. Chen, B. Dong, S. Lu, A. Abdelkader, Y. Guo, Y. Zhang, S. Ding, K. Xi, G. Gao, *J Mater Chem A Mater* 2017, *5*, DOI 10.1039/c7ta02136d.
[54]   V. Marangon, K. Bischof, A. A. Regalado, M. Keppeler, M. Pogosova, M. Wan, J. Choi, S. Fleischmann, T. Diemant, M. Wohlfahrt-Mehrens, M. Hölzle, T. Waldmann, D. Bresser, *J Power Sources* 2025, *634*, DOI 10.1016/j.jpowsour.2025.236496.
[55]   N. Yabuuchi, K. Kubota, M. Dahbi, S. Komaba, *Chem Rev* 2014, *114*, DOI 10.1021/cr500192f.
[56]   M. A. Muñoz-Márquez, M. Zarrabeitia, E. Castillo-Martínez, A. Eguía-Barrio, T. Rojo, M. Casas-Cabanas, *ACS Appl Mater Interfaces* 2015, *7*, DOI 10.1021/acsami.5b01375.
[57]   C. D. Wagner, *Faraday Discuss Chem Soc* 1975, *60*, DOI 10.1039/DC9756000291.
[58]   Z. W. Seh, J. Sun, Y. Sun, Y. Cui, *ACS Cent Sci* 2015, *1*, DOI 10.1021/acscentsci.5b00328.
[59]   H. S. Hirsh, B. Sayahpour, A. Shen, W. Li, B. Lu, E. Zhao, M. Zhang, Y. S. Meng, *Energy Storage Mater* 2021, *42*, DOI 10.1016/j.ensm.2021.07.021.
[60]   H. Seyama, M. Soma, *Journal of the Chemical Society, Faraday Transactions 1: Physical Chemistry in Condensed Phases* 1985, *81*, DOI 10.1039/F19858100485.
[61]   J. Duan, W. Wang, D. Zou, J. Liu, N. Li, J. Weng, L. P. Xu, Y. Guan, Y. Zhang, P. Zhou, *ACS Appl Mater Interfaces* 2022, *14*, DOI 10.1021/acsami.2c04831.
[62]   K. Zou, W. Deng, D. S. Silvester, G. Zou, H. Hou, C. E. Banks, L. Li, J. Hu, X. Ji, *ACS Nano* 2024, *18*, DOI 10.1021/acsnano.4c02307.
[63]   P. R. Griffiths, *Vib Spectrosc* 1992, *4*, DOI 10.1016/0924-2031(92)87021-7.

Data availability

The data supporting this article have been included as part of the Supplementary Information.